Moho depth and crustal thinning in the Marmara Sea region from gravity data inversion

J. Kende, P Henry, G. Bayrakci, M. Özeren, C. Grall

Key Points:
- Gravity data corrected from the sedimentary basins are inverted to build a Moho topography
- The 3-D crust model obtained is used to compute the total extension in the area, and the result is compared with current extension rate
- Comparing the basins/Moho geometry, the ductile lower crust flow that could account for the broad thinning south of the NMT is evaluated

Moho depth and crustal thinning in the Marmara Sea region from gravity data inversion

J. Kende[1] (iD), **P. Henry**[1] (iD), **G. Bayrakci**[2], **M. S. Özeren**[3], **and C. Grall**[4]

[1]CEREGE, Aix-Marseille Université, CNRS, IRD, Collège de France, Aix en Provence, France, [2]Ocean and Earth Science, National Oceanography Centre, University of Southampton, Southampton, UK, [3]Maden Fakültesi, İstanbul Teknik Üniversitesi, İstanbul, Turkey, [4]Marine Geology and Geophysics, Lamont-Doherty Earth Observatory, Columbia University, New York, New York, USA

Abstract The free-air gravity in the Marmara Sea reveals that the low density of sedimentary basins is partly compensated in the lower crust. We compiled geophysical upper crust studies to determine the sediment basin geometries in and around the Marmara Sea and corrected the gravity signal from this upper crust geology with the Parker method. Then, assuming long wavelength anomalies in the residual gravity signal is caused by variations in the Moho topography, we inverted the residual to build the Moho topography. The result shows that the Moho is uplifted on an area greater than the Marmara Sea with a maximum crust thinning beneath the basins where the Moho is at about 25 km, 5 km above the reference depth. We then evaluated the Neogene extension by comparing the surface covered by our 3-D thinned model with the surface covered by an unthinned model with same crustal volume. Comparing this surface with areal extension rate from GPS data, we found a good compatibility indicating that the extension rate averaged over the Sea of Marmara area probably remained close to its present-day value during major changes of tectonic regime, as the incursion of the North Anatolian Fault system during the Pliocene leads to the establishment of the dominantly strike-slip present-day system. We also show that crustal extension is distributed over a wider domain in the lower crust than in the upper crust, and that this may be accounted for by a relatively minor component of lower crustal ductile flow.

1. Introduction

Basin formation along strike-slip fault zones generally results from crustal extension at a releasing bend or releasing overstep [e.g., *Christie-Blick and Biddle*, 1985; *Biddle and Christie-Blick*, 1985]. The rheology of the lower crust and the ratio of step over width to brittle crust thickness thus appear as essential parameters controlling the distribution of extension, basin geometry, and sediment thickness [*Petrunin and Sobolev*, 2006; *Smit et al.*, 2008]. With this respect, the Dead Sea and the Death Valley have been considered as end-member cases. The Dead Sea pull apart corresponds to a small 10 km step over in a mostly brittle 35 km crust, in which case the extension occurs along the basin axis and remains confined in the narrow corridor defined by the bounding strike-slip faults [*Katzman et al.*, 1995; *Petrunin and Sobolev*, 2006; *Ten Brink et al.*, 1993]. The Death Valley fault corresponds to a more than 50 km step over in a relatively thin brittle crust, in which case the basin developed as an oblique structure bounded by normal faults [*Burchfiel and Stewart*, 1966]. Remarkably, in both cases, the Moho is not uplifted beneath the basins for contrasted reasons. The Dead Sea basin is essentially uncompensated, with little involvement of the mantle in the formation of the basin [*Ten Brink et al.*, 1993; *Petrunin and Sobolev*, 2006]. Below the Death Valley, the crust is hot and highly ductile, affected by the regional basin and range extension, resulting in compensation within the crust and a flat Moho [*De Voogd et al.*, 1988; *Fliedner et al.*, 1996]. The Marmara Sea corresponds to an intermediate case where the step width is comparable to the width of the brittle crust (15–20 km), as may be estimated from the depth distribution of earthquakes [*Schmittbuhl et al.*, 2016], and wide-angle refraction studies indicate a Moho at 26 km depth below sea level beneath the Marmara Sea troughs, implying at least 5 km of uplift [*Bécel et al.*, 2009]. Compared to the Dead Sea low heat flow, estimated less than $50 \, \mathrm{mW \, m^{-2}}$ [*Ben-Avraham et al.*, 1978; *Garfunkel and Ben-Avraham*, 1996], and the heat flow above $100 \, \mathrm{mW \, m^{-2}}$ of the Death valley [*Sass et al.*, 1994], the Marmara Sea, with a crustal heat flow ranging between 55 and $85 \, \mathrm{mW \, m^{-2}}$ [*Grall et al.*, 2012; *Pfister et al.*, 1998], appears as intermediate and representative of average continental crust heat flow [*Pollack et al.*, 1993]. The Marmara Sea case may thus provide some insight on the influence of crustal heat flow and rheology on strike-slip basin development and associated crustal thinning, hence motivating the present study.
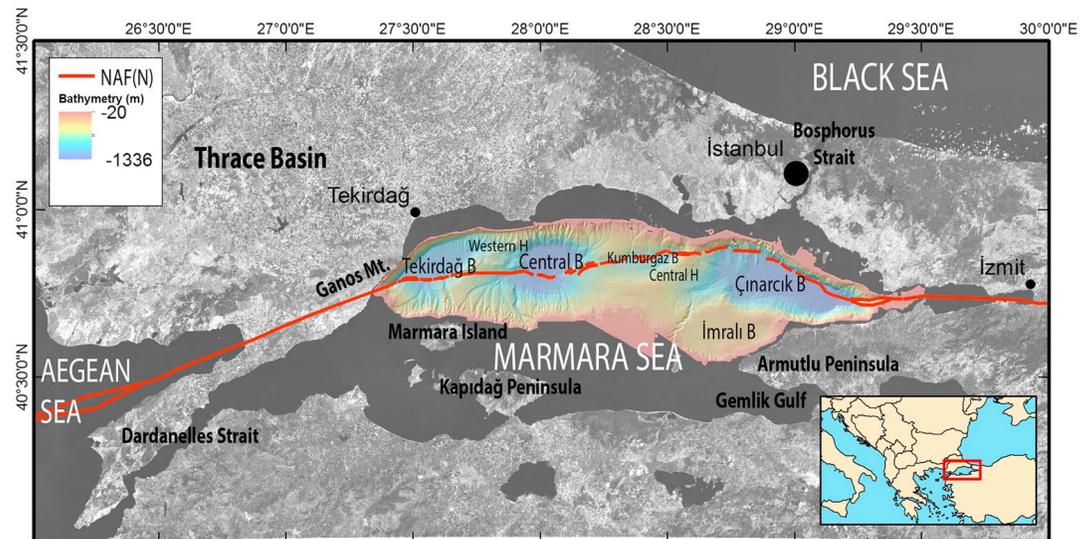
Figure 1. Geographic and simplified tectonic setting of the Marmara Sea. B stands for Basins, H for Highs, and NAF(N) for the northern branch of the North Anatolian Fault. The Fault location is modified from *Şengör et al.* [2014]. Bathymetry data are from the EM300 multibeam survey.

The Marmara Sea is situated along a segment of the North Anatolian Fault (NAF), a vast fault system carrying 20 to 27 mm/yr of dextral strike-slip motion, according to GPS, between the Anatolian and the Eurasian plates [*Reilinger et al.*, 2006; *Hergert and Heidbach*, 2010]. In its western part, the NAF splits into several branches. The Marmara Sea overlies the NAF northern branch, the Main Marmara Fault (MMF) [*Le Pichon et al.*, 2001; *Şengör et al.*, 2005] (see Figure 1). While the MMF is interpreted as a pure, or dominantly, strike-slip fault [e.g., *Rangin et al.*, 2004; *Seeber et al.*, 2004], there are remaining uncertainties about the amount of extension taken up in the Marmara Sea region and about the extensional mechanisms that led to the present basin geometries. *Bécel et al.* [2009] interpreted a northward dipping seismic reflector as a detachment oriented N40°E south of the Central Basin and suggested an asymmetric crustal thinning toward the SW. In the same study, *Bécel et al.* [2009] identified *Pn* wave, refracted on top of the upper mantle, in wide-angle seismic data and showed that the crustal thinning spreads southward over a broader domain than the deep basins composing the North Marmara Trough (NMT). This result has been confirmed by a north to south onshore seismic survey [*Karabulut et al.*, 2013], cutting the Marmara Sea at about the Marmara Island longitude and showing a smooth 5 km thinning over a zone wider than the Marmara Sea.

We conducted a gravity data analysis, using seismic study results as constraints [*Bécel et al.*, 2009; *Karabulut et al.*, 2013; *Bayrakci et al.*, 2013], to produce a Moho depth map, draw a budget of crustal extension, and evaluate the lower crustal ductile flow contribution to the extension processes.

2. Data

2.1. Gravity and Topographic Data

The gravity anomaly map used in our study was obtained by merging a global gravity model and marine ship data acquired in the Marmara Sea. First, we retrieved a gravity grid from the Scripps Institution of Oceanography website. Available on http://topex.ucsd.edu/WWW_html/mar_grav.html, the data grid is based, for the marine domain, on past 3×10^{-5} to 4×10^{5} m s^{-2} (3 to 4 mGal) accurate Geosat and ERS-1 satellites data and new altimeter data from Jason-1 and CryoSat-2 satellites, with the later providing the dense coverage of a 2.5 km track spacing [*Sandwell and Smith*, 1997; *Sandwell et al.*, 2014]. The estimated accuracy at the Marmara Sea latitude is about 1.7×10^{-5} m s^{-2} [*Sandwell et al.*, 2013]. The land part of this global model is based on the Earth Gravitational Model 2008 [*Pavlis et al.*, 2012]. A linear interpolation was used to refine the map in order to obtain a 256×512 cell grid covering the considered area and appropriate for fast-Fourier transform, which is optimized for grid sizes that are powers of 2. The area of our study covers latitudes between 40° and 41.5° and longitudes between 26° and 30°.
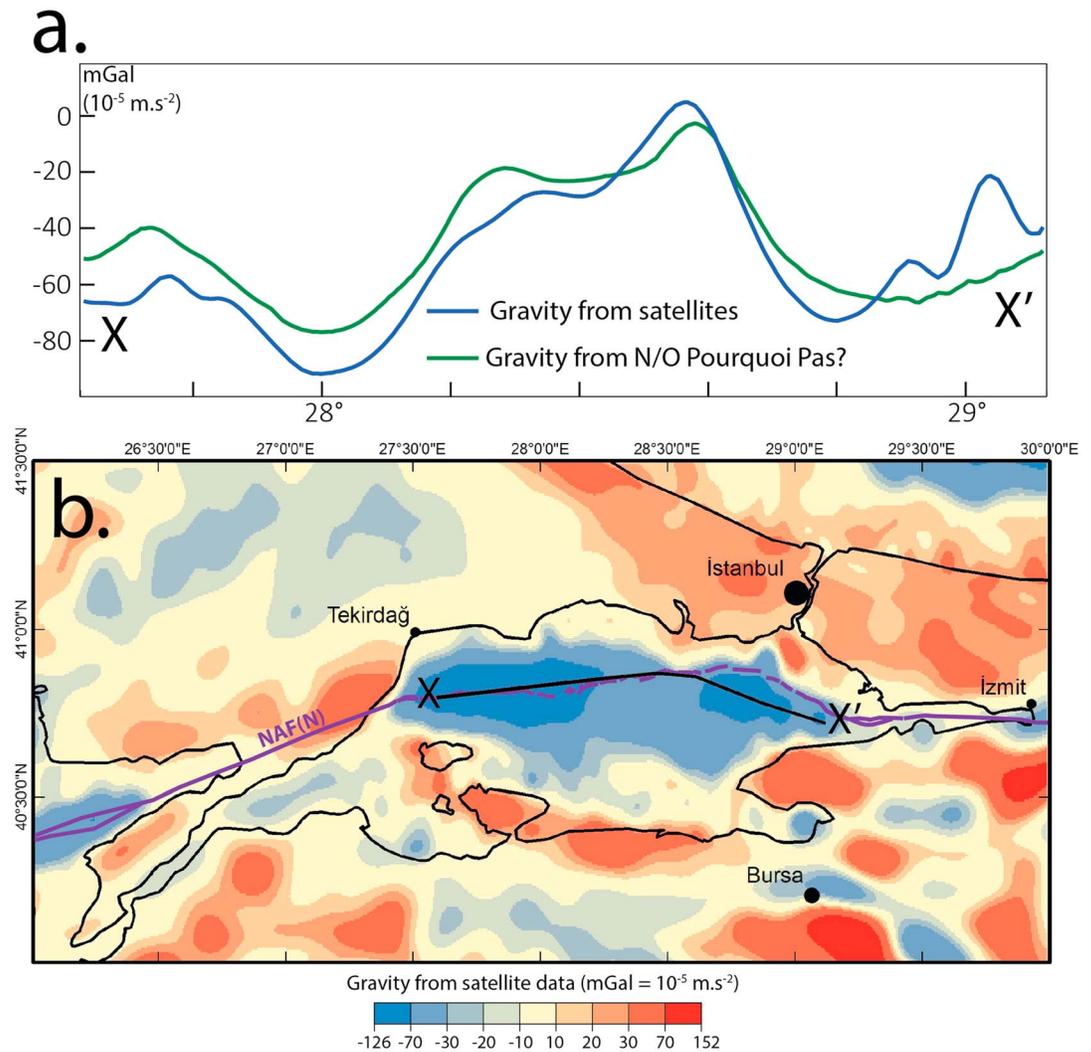
Figure 2. (a) Comparison of free-air gravity data from satellite altimetry [*Sandwell et al.*, 2014] and from N/O *Pourquoi Pas?* shipboard gravimeter on a transection. (b) Free-air anomaly field interpolated from satellite data only and location of the transect shown in Figure 2a.

The second data source is the gravity data collected during the Marsite Cruise in October and November 2014 on board the survey vessel N/O *Pourquoi Pas?*. The ship is equipped with a Bodenseewerk KSS 31 gravimeter working with a spring on a stabilized platform. The device is installed at the ship steadiest spot and records data at a high time resolution giving a space resolution of about 1 m. As the data we accessed are not calibrated at port station, the mean value of the ship data was moved to match the satellite data mean value in the Marmara Sea. Then a 256×512 cell grid covering our area of study was created from the ship data with linear interpolation and extrapolation from the closest value.

Figure 2 shows a comparison of the two data sources on a transect, as well as the satellite data grid with the transect location. The inconsistency visible in the east probably corresponds to a location where the spline interpolation of the satellite data creates short wavelet oscillations. Another feature that will be removed when integrating the ship gravity data is the negative anomaly near the Bosphorus Strait. The high speed of the jet current at the Bosphorus outlet (about $2\,\mathrm{m\,s^{-1}}$) results in negative sea topography. This local lowering of the sea surface results in an apparent gravity low in the satellite gravity map.

The data were combined by using the grid created from ship data within 1700 m of the ship track and the grid from satellite data further than 4200 m. The corridors in between were filled by a biharmonic spline interpolation available in MATLAB and based on *Sandwell* [1987]. Figure 3 shows our final free-air gravity
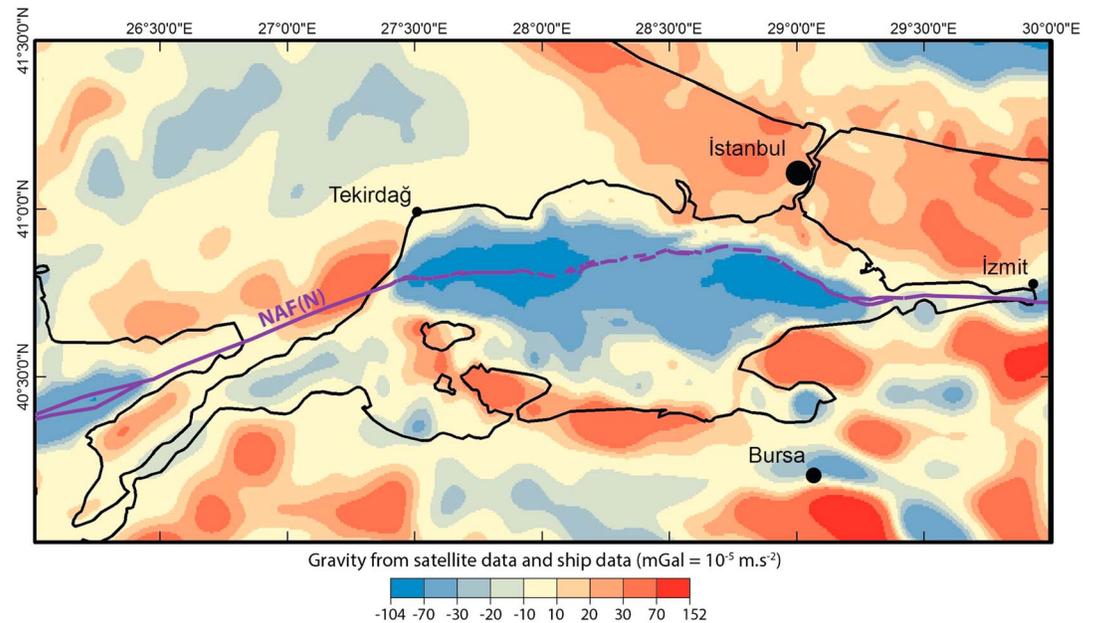
Figure 3. Final free-air anomaly map combining the satellite data and the Marsite cruise gravity measurements.

map. The merging delivered finer data in the Marmara Sea and eliminated small artifacts in the eastern part of the Marmara Sea (see Figure 2). However, as the ship tracks were not evenly spaced over the entire study area, artifacts may remain in the final grid.

The bathymetric data used for the Marmara deep basins, presented in Figure 1, is based on the EM300 multibeam survey of the Marmara Sea basins [*Le Pichon et al.*, 2001]. On the shelves and on land, we used the global topographic grid available from the Scripps Institution of Oceanography website.

2.2. Sediment Thickness Data

The basin model used in this study is mostly based on the sediment thicknesses derived from the tomographic study presented in *Bayrakci et al.* [2013]. We adopted the distinction of a synkinematic layer and a prekinematic layer first introduced by *Laigle et al.* [2008] and corresponding, respectively, to the sediments deposited during and before the opening of the Marmara basins. *Laigle et al.* [2008] identified the boundary between the two layers, while *Bayrakci et al.* [2013] estimated that the 4.2 km s^{-1} and 5.2 km s^{-1} P wave velocity isocontours delimit them.

The velocity/density model is probably more complex and heterogeneous in details. The presence of a damaged zone with low seismic velocities and negative density anomalies has been observed around the North Anatolian Fault east of the Marmara Sea [*Ben-Zion et al.*, 2003] and in the San Andreas fault zone area [e.g., *Feng and McEvilly*, 1983; *Wang et al.*, 1986]. It is very likely that a damage zone associated with density contrasts also occurs in the Marmara Sea, for instance, between the NMT and its surrounding. However, the seismic surveys on which the basin model is based do not show clear evidence for this, and the resolution of the gravity data is also too low to account for such contrasts.

The sediment thickness model was extended over the southern shelf based on interpretation of multichannel seismic profiles provided by the Turkish Petroleum company [*Le Pichon et al.*, 2013]. In this interpretation, Plio-Quaternary sediments are distinguished from prekinematic Miocene to early Pliocene sediments, which are deposited on basement or cretaceous carbonates. P wave velocity, as described in *Bayrakci et al.* [2013], was also considered when known.

In order to limit edge effects in the gravity inversion, the area of interest is not limited to the Marmara Sea. Nearby structures had to be modeled as well: the Black Sea and the Thrace basin.

Only the southwestern part of the Black Sea was included in the domain of study. The sediment layers were extrapolated from the profile presented on Plate 14 in *Robinson et al.* [1996] by adopting a constant thickness
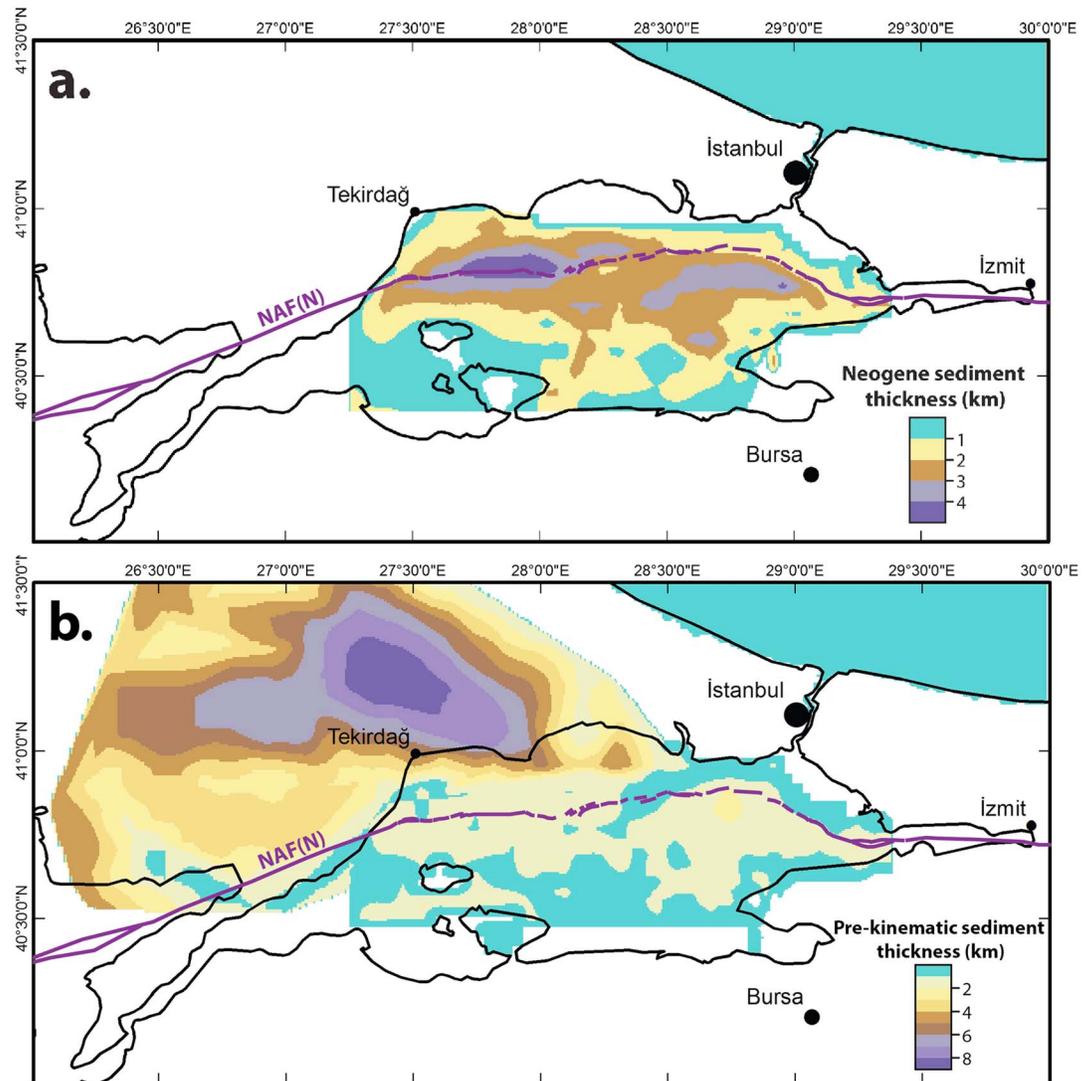
Figure 4. Thickness of the two sediment layers expended from *Bayrakci et al.* [2013] model defined between 27.25°–29.4°E and 40.5°–41.1°N. The layers initial definition is based on *P* wave velocity. The synkinematic sediment layer corresponds to velocities lower than 4.2 km s^{-1}, and the prekinematic sediment layer has *P* wave velocities comprised between 4.2 km s^{-1} and 5.2 km s^{-1}. *Bayrakci et al.* [2013] model was expanded interpreting the bottom of the Plio-Quaternary sediments as the interface between the two layers when *P* wave velocities were not available. Plio-Quaternary sediment thickness is neglected in the Thrace basin, and a simple model with constant thickness is applied to the Black Sea.

of 600 m for the first as well as for the second layer of sediment. Thus, we obtain sediment depths directly related to the bathymetry. Although this is a rough approximation of the Black Sea sedimentary structure, this approximation does not strongly affect our model in the Marmara Sea area.

The Oligocene-Eocene Thrace basin geometry is well constrained from seismic surveys and industry boreholes. We used the sediment depth model presented in *Siyako and Huvaz* [2007] and mainly based on well data [*Huvaz et al.*, 2007]. We ignored the Plio-Quaternary sediment layer as its thickness is always less than 500 m [*Siyako and Huvaz*, 2007].

Finally, the two sediment depth maps were refined using a linear interpolation in order to obtain a 256 × 512 cell grid matching the gravity data grid. Figure 4 shows the final thickness map for the two sediment layers.

2.3. Crustal Structure

The existence of a reflective lower crust has been shown by both multichannel seismic [*Laigle et al.*, 2008] and ocean bottom seismometer [*Bécel et al.*, 2009] data. However, the deep reflections could only be identified on

few multichannel seismic profiles due to the multiples or lateral echoes. The top of the lower crust, as well as the Moho, are therefore constrained by wide-angle refraction-reflection data recorded by far offset stations and few Ocean Bottom Seismometers (OBSs) that provide enough depth penetration. *Bécel et al.* [2009] imaged the top of the lower crust on three 2-D profiles and proposed a 2-D model where the lower crust and the Moho have a similar geometry, with the upper/lower crust interface lying at two thirds of the Moho depth. We assume that the continental crust retains these proportions in the modeled domain in 3-D, as we do not have any other independent data to constrain the 3-D model. The geometry of the interface between the upper and the lower crust will thus be calculated together with the geometry of the Moho using the inversion method detailed below. The calculated Moho and the upper/lower crust interface depths will then be compared to available constraints from seismic studies.

3. Method

Modeling the Moho depth variations from gravity data is a two-step process. First, the impact of the known geology and topography on the gravity must be accounted for and removed from the free-air gravity. The resulting gravity anomaly represents the effect of density variations in the deeper part of the crust and in the mantle. We assumed that the remaining anomalies are related to Moho depth variations and can be inverted to determine the geometry of the Moho.

For the first step, we computed the effect of our upper crust model on gravity in the onshore and offshore domains.

3.1. Gravity Correction Over the Onshore Domain

For the onshore domain, we first applied a Bouguer correction to remove the effect of the topography. In the Thrace basin, we used a sediment density for the Bouguer calculation equal to the density of the prekinematic sediment layer and then corrected for the Thrace basin sediment thickness using the same procedure as for the offshore domain.

Prior to computing the Bouguer correction, a Gaussian filter with a 20 km window was applied on the topography. This filtering was needed because wavelengths shorter than 20 km are absent from the satellite gravity grid. This filtering does create a risk of interfering with crustal effect on gravity and losing part of the signal [*Aitken et al.*, 2013].

3.2. Gravity Correction in the Marmara Sea, in the Black Sea, and in the Thrace basin

The Bouguer correction is a fast and effective approximation of the gravity anomaly caused by topography on land. But, as we need to account for the effect of the Marmara Sea basins, the gravity must be corrected from the influence of the bathymetry variations and from the effect of water and sediment layers:

$$g_{corrected} = g_{measured} - \delta g_w - \delta g_{S_1} - \delta g_{S_2}$$

where δg_w, δg_{S_1}, and δg_{S_2} are the effect on gravity of, respectively, the layer of water, the synkinematic sediments, and the prekinematic sediments.

The basin correction was performed through the application of the Parker method [*Parker*, 1972], which is based on a Fourier transform of the gravity equation:

$$F[g(x)] = -2\pi G \Delta\rho e^{-|k|z_0} \sum_{n=1}^{\infty} \frac{|k|^{n-1}}{n!} F[h^n(x)] \qquad (1)$$

where $\Delta\rho$ is the density difference at the considered interface, k is the wave number of the transform function, and z_0 is the mean depth of the considered interface. $F[g(x)]$ and $F[h^n(x)]$ are, respectively, the Fourier transform of the gravity field and of the interface depth.

We used the Parker equation to calculate the gravity correction based on our three interfaces: the water/synkinematic sediment interface, the synkinematic/prekinematic sediment interface, and the prekinematic sediment/crust interface. We obtain the gravity correction to be applied on the observed gravity field to account for differences between our model and an ideal model with a flat topography and no sedimentary basins.

In the Thrace basin, we have the special case of a sedimentary basin with a positive topography. The Bouguer correction accounted for the positive topography, and the Parker method accounted for the sedimentary basin below sea level.

3.3. Residual Anomaly Inversion and Moho Depth Variation Determination

Methods for determining the Moho variations and crustal thickness from gravity data have been used for more than a century [e.g., *Vening-Meinesz*, 1931]. Approaches include inversion, forward modeling, process-oriented modeling, and spectral analysis (see *Aitken et al.* [2013] for a review).

Here we developed a fast inversion method, close to the Parker-Oldenburg algorithm [*Oldenburg*, 1974]. First, the Parker equation was linearized, retaining only the first term of the Taylor development:

$$F[g(x)] = -2\pi G\Delta\rho e^{-|k|z_0} F[h(x)] \tag{2}$$

This equation direct inversion is

$$F[h(x)] = -\frac{e^{|k|z_0}}{2\pi G\Delta\rho} F[g(x)] \tag{3}$$

This equation would not yield satisfactory results for the Moho because the high wave number terms are amplified, while in fact they are unconstrained by data at wavelengths shorter than the crustal thickness. The method we propose is preconditioning to 0 the amplitude of Moho variations. A least squares misfit function is thus defined in the Fourier domain as

$$S[h] = \frac{1}{2\pi G\Delta\rho} \|F[g](k) - F[g_{\text{obs}}](k)\|^2 + \left\|\frac{F[h](k)^2}{\sqrt{C(k)}}\right\| \tag{4}$$

where the covariance diagonal matrix $C(k)$ scales the model deviation from the a priori model (flat Moho) with the error on data projected in the model space [*Tarantola*, 2005]. We will assume $C(k)$ constant, independent of wave number. At short wavelengths, the first term is nearly independent of the model, and at the minimum of S, $h(k) \approx 0$. For long wavelengths, the first term becomes dominant, and the preconditioning has little effect on inversion results. The solution of this linear least squares problem is [*Tarantola*, 2005]

$$F[h(x)] = \frac{1}{2\pi G\Delta\rho} \left(e^{-|k|z_0} \times e^{-|k|z_0} + \frac{1}{C}\right)^{-1} \times e^{-|k|z_0} \times F[g_{\text{obs}}(x)] \tag{5}$$

This is equivalent to applying a low-pass filter to the linearly inverted Moho, where C controls the cutoff wavelength. One theoretical advantage of this method is that the shape of the filter is consistent with a preconditioning approach [*Tarantola*, 2005].

The low-pass filter corresponds to

$$\text{filter} = \left(e^{-|k|z_0} \times e^{-|k|z_0} + \frac{1}{C}\right)^{-1} \times e^{-2|k|z_0} = \left(1 + \frac{e^{-2|k|z_0}}{C}\right)^{-1} \tag{6}$$

The passband power is met when $k = 0$ and we can define a cutoff wave number k_c corresponding to k for which the output is half of the passband power

$$k_c = \frac{\ln(C)}{2z_0} \tag{7}$$

3.4. Modeling Parameters

Using an inverse modeling method is a fast, effective, and repeatable way to compute a model on a large area with a fine gridding. It also removes part of human biases that are a risk when carrying forward modeling in which the model is manually modified until it fits a set of conditions that describe an acceptable Moho and meets the geophysical observations [*Aitken et al.*, 2013]. However, the whole model is based on the acceptance of the initial shallow geologic setting, on the precision of the topographic and gravimetric surveys and on the few parameters that are user input: the layer densities, the reference Moho depth, and the covariance parameter for the Moho inversion.

The geologic model we first used consisted of five layers, each characterized by a density: water, first sediment layer (synkinematic), second sediment layer (prekinematic), crust, and mantle.

The crust and mantle density were chosen based on *Bécel et al.* [2009] *P* wave velocities and on *Sobolev and Babeyko* [1994] *P* wave velocity versus density curves. We chose a density of 2650 kg m^{-3} for the upper crust as the *P* wave velocities at the top and bottom of the layer are 6 and 6.2 km s^{-1}. The lower crust *P* wave velocity is 6.7 km s^{-1}, corresponding to 2950 kg m^{-3}. The values retained are also compatible with *Christensen and Mooney* [1995] average velocity versus average density curve. Seismic velocity models do not indicate that the proportion of upper and lower crust varies significantly or that lateral variations of density are present in each layer. With two third of upper crust and one third of lower crust we obtain an average density value of 2750 kg m^{-3} for the whole crust. Mantle density is taken equal to 3330 kg m^{-3}.

An upper/lower crust interface is included in the gravity model. The interface is defined at two thirds of the Moho depth. The location of the interface is thus calculated iteratively, until convergence is reached, from the depth of the Moho (inversion result). The results obtained with this layered crust model are not exactly identical to those obtained with a single layer crust of density 2750 kg m^{-3}, but the difference is small: taking into account the upper/lower crust interface lowers the standard deviation of the final residual anomaly in the domain of study by about 0.6×10^{-5} m s^{-2} (0.6 mGal).

The synkinematic and prekinematic sediment thicknesses that we adopted from *Bayrakci et al.* [2013] model are identified with *P* wave isovelocity contours: the first layer refers to the field in which *P* wave velocity is smaller than 4.2 km s^{-1} and prekinematic sediments have *P* wave velocities between 4.2 km s^{-1} and 5.2 km s^{-1}. To estimate the two sedimentary layer densities from these velocities, we used *Erickson and Jarrard* [1998] relation for siliciclastic water-saturated sediments:

$$V_p = 1.11 + 1.178\varnothing + \frac{0.305}{\left[(\varnothing + 0.135)^2 + 0.0725\right]} + 0.61(v_{sh} - 1)(X - \mathrm{abs}(X))$$

where $X = \tanh(20(\varnothing - 0.39))$. V_p is the compressional wave velocity, v_{sh} the shale fraction, and $\varnothing$ the porosity.

It has the advantage of including the shale fraction as a variable which allows us to evaluate reasonable uncertainties since sediments may change from very fine clay to coarser layers. We tested the relation with v_{sh} varying from 0 to 1. For a velocity of 4.2 km s^{-1}, we obtained the limit values of 2400 kg m^{-3} ($\varnothing = 0.15$) and 2630 kg m^{-3} ($\varnothing = 0.01$), using 2650 for siliciclastic grain density. One should note that the value calculated with $v_{sh} = 1$ largely encompass the possible drifting described by *Erickson and Jarrard* [1998] when dealing with very low porosities. Then considering a porosity for shallow clay rich sediments of 700 kg m^{-3} [*Le Pichon et al.*, 1990], which is consistent with measurements on Marmara Sea sediment cores [*Aloisi et al.*, 2015], and an exponential porosity-depth law (Athy's law, [*Grall et al.*, 2012, 2013]) from the sediment layer top to its floor, we obtain a range of 2070 to 2390 kg m^{-3} for the average density of the first layer of sediment.

For the bottom limit of the second layer, we used the same equation and $v_{sh} = 0$ to determine a minimum density of 2600 kg m^{-3} ($\varnothing = 0.03$). From this value and the one calculated at the layer top, we get an average minimum density for the second layer of sediment of 2530 kg m^{-3} ($\varnothing = 0.07$). We then consider 2650 kg m^{-3} as a maximum, for which there is no density contrast between the second layer of sediment and the upper crust.

The two ranges of density were scanned with a step of 20 kg m^{-3}, and all combinations were tested. Each time, we calculated the residual gravity after correcting for the Marmara Sea basins without taking into account the Thrace basin and the Black Sea sediments.

The comparison of the residual standard deviations indicates that the higher the density values are, the smaller the residual gravity anomaly is. If a homogeneous crustal density is assumed for the upper crust and the two sediment layers (2650 kg m^{-3}), the residual anomaly is very small, which would result in an almost flat Moho. However, this interpretation can be considered unrealistic in view of the seismic data. Nevertheless, the residual anomaly and calculated Moho geometry are strongly dependent on the average densities assumed for the sedimentary layers.

In the following, the discussion will be based on a mean model obtained with average density values of 2230 and 2590 kg m^{-3} for synkinematic and prekinematic sediments, respectively. We will also consider that

varying the density within the determined range yields the possible range of variation of Moho depth maps as constrained by gravity.

For the inversion of the corrected gravity field, two more parameters have to be set: the mean Moho depth and the covariance. The choice of the mean Moho depth was based on *Karabulut et al.* [2013] and set to 30 km. We preferred that value to the about 35 km depth inferred around the Marmara Sea in *Bécel et al.* [2009] as their distribution of receiver and sources does not constrain well the Moho depth outside the basins. It is also the reference value chosen by *Tiberi et al.* [2001] for their inversion of gravity data after correcting for the plunging African slab in the Corinth Rift area.

The covariance parameter has a direct impact on the Moho results. We tested covariance ranging from 10 to 50 and selected 25 as it gives the depth variation amplitude closest to the one observed by *Karabulut et al.* [2013] for the model with intermediate gravity values. This corresponds to a cutoff wavelength of about 120 km.

4. Results

Figure 5 shows the intermediate result of the gravity field corrected from the topography and the upper crust density variations, before inversion. Figure 6 shows the Moho depth and the final residual, which is the difference between the measured gravity and the modeled gravity. Results computed with the minimum and maximum sediment densities within the bounds we defined are also presented. Although the Moho depth variation amplitude changes, the geometry is very similar on results a and b and all three results show a "saddle" shaped Moho. The thinning spreads farther north than south of the Marmara Sea, considering 30 km depth as the default depth in a homogeneous crust, and the two shallowest zones are centered north of the Marmara Island and above the Çınarcık basin. The RMS of the difference between the depths of the two extreme models is 1 km. Hence, the model is fairly robust to variations of the sediment densities within the reasonable bounds we defined.

The modeled gravity is the summation of on-land Bouguer correction, basin effects on the gravity, and the gravity anomaly produced by the inferred Moho and upper crust/lower crust boundary. Thus, observation of the gravity residual is representative of the model accuracy as it is the part of the gravity measurement not explained by our model.

As presented in Figure 6, with each of the sediment density pair inputs, we obtain a map with a residual gravity anomaly equal to $0 \pm 5 \times 10^{-5}\,\mathrm{m\,s^{-2}}$ (0 ± 5 mGal) on the majority of our domain of study.

In the Marmara Sea, the residual is characterized by a positive "belt" spreading from east to west above the basins and along the southern shore. In the middle, the Marmara Island, the zone north of the Kapıdağ Peninsula and the İmralı basin, are small areas with negative residuals. We will discuss separately the northern and the southern part of the positive belt as they probably result from two different mechanisms.

The northern part of the belt coincides with the deep basins and shows the highest residuals at the location of the current depocenters in the Tekirdağ and the Çınarcık basins. This may be due to the fact that sediment layers are characterized by only one mean density, which may be too small for zones with a very thick sediment layer. Similarly, as the residual above the basins is decreased by highest density values, the density ranges we defined earlier may be overly shifted toward lower density values. Also, in this zone, the positive residual creates a pattern which coincides with the Marsite cruise ship path. Thus, although the merging of the N/O *Pourquoi Pas*? and the satellite data suppressed an artifact in the east (see Figure 3), the two data source may not be consistent enough. We could probably lower this positive residual by normalizing the ship data with regards of the satellite data, instead of only matching the averages. But the area covered by the ship data is not wide enough to be representative and to allow such a correction. Part of the positive residual is also due to the fact that wavelength shorter than the geological model resolution is not compensated and cannot be lessened when adding the Moho interface. So short wavelength gravity variations are visible where they were recorded along the ship path.

The southern part of the positive belt, which spreads along the southern shore, coincides with a positive gravity anomaly in the initial gravity data (see Figure 3). The preservation of this positive anomaly as a residual, independent of the sediment densities, indicates that our model probably lacks a structure which should
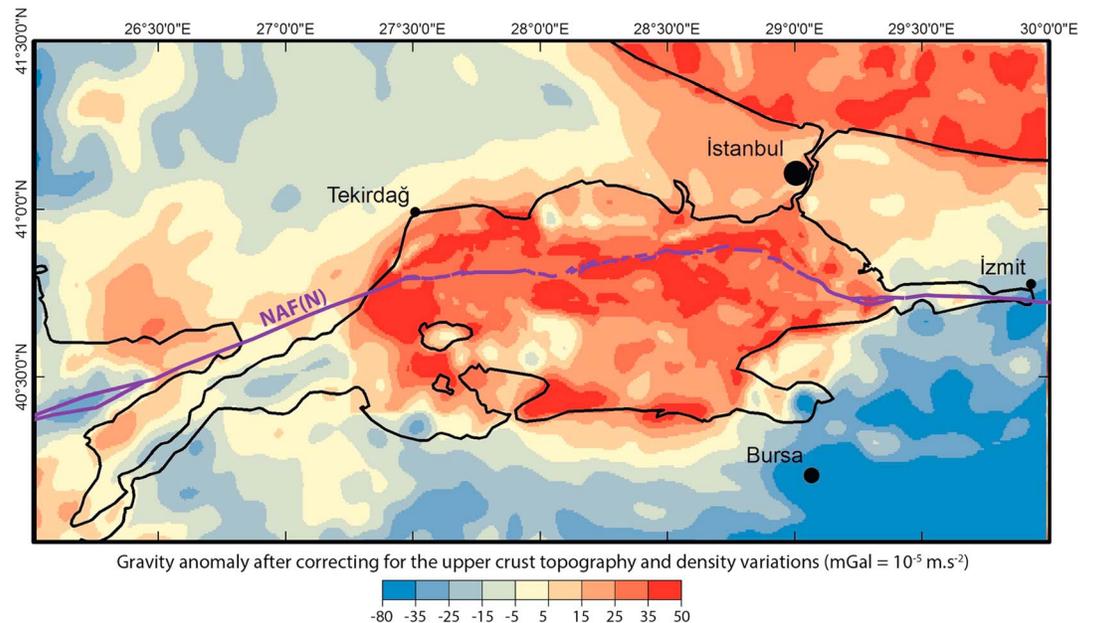
Figure 5. Gravity anomaly after correcting the measured gravity field using Bouguer calculation for the topography and the Parker method [*Parker*, 1972] for the sediment basins.

account for it. For instance, it could be an elastic flexure effect inside the upper crust related to the tilted blocks in the southern basins [*Bécel et al.*, 2009], as we have no constraint on the upper crust at that location.

Away from the Marmara Sea, at the limits of the area of study in the north-east and south-east directions, the overly bended Moho indicates an edge effect due to the fact that the Moho is approximated with Fourier transforms. This problem will not be discussed further as the area is large enough to avoid such effect near the Marmara Sea.

4.1. Compatibility With Published Geophysical Studies

To assess the accuracy of our model, we here compare our results with previously published Moho depth data from geophysical surveys: *Bécel et al.* [2009] profiles based on Multichannel reflection Seismic (MCS) lines, on-land stations and OBSs, and *Karabulut et al.* [2013] 650 km long north-south profile based on a tomographic study. As the parameters in our study were chosen in order to reach a model close to those constructed by these geophysical surveys, it is expected that amplitude and main structures are alike. We will discuss the remaining differences.

In *Bécel et al.* [2009], three profiles based on marine multichannel reflection seismic, Ocean Bottom Seismometers (OBSs), and onshore reflection/refraction records are presented. Figure 7 shows a comparison of these three profiles and of our results.

In wide-angle refraction-reflection modeling, reflections give information about the topography of the interfaces whereas refractions constrain the velocity of the medium, which in turn has an effect on the depth of the interfaces. On the far offset stations, the reflections from the top of the lower crust (PiP) and Moho (PmP) are clear. However, at the edges of the profiles, due to the sparse refraction sampling and the velocity-depth ambiguity, the depth of the interfaces is expected to be less accurate than in the regions sampled abundantly by both reflections and refractions (e.g., below the NMT the top of the crystalline crust is sampled abundantly by reflections from the basement and by refracted waves within the basement). Furthermore, even if *Bécel et al.* [2009] positioned the Moho at about 35 km away from the basin, this is an a priori depth and they found evidence only for 5 km of absolute Moho depth variation. Thus, we will focus on comparing the profiles under the NMT, where it is best constrained by seismic data.

The AA′ profile [*Bécel et al.*, 2009] under the NMT shows a thinning almost constant under the main basins. Our 3-D model is consistent with this 2-D model under the basins, with a Moho depth at about 25 km and a slightly thicker crust in the central part of the Marmara Sea.
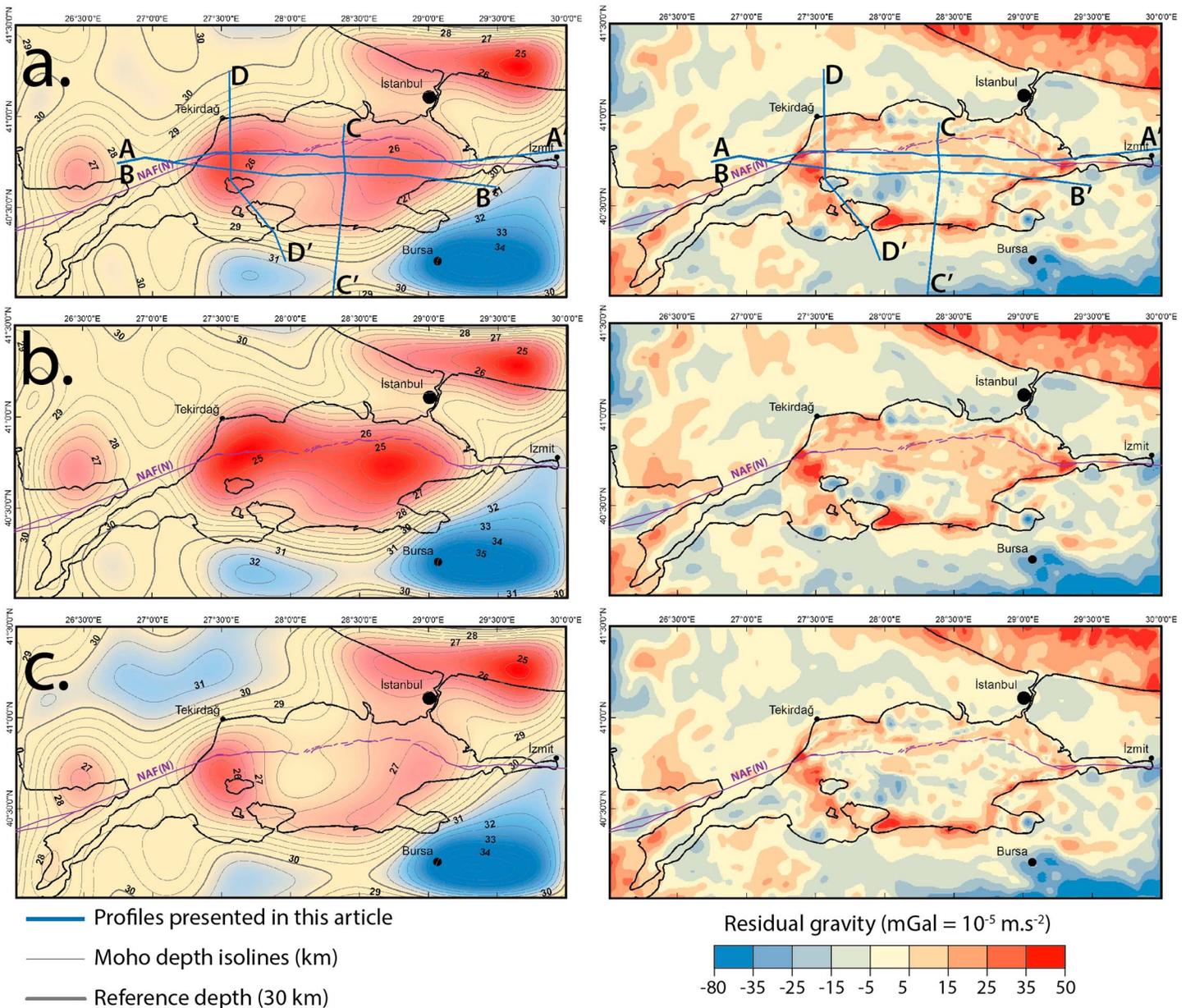
Figure 6. Moho depth topography and gravity residual computed with variable density for the synkinematic sediment layer and the prekinematic sediment layer with, respectively, (a) 2.23 and 2.59 g cm^{-3}, (b) 2.07 and 2.53 g.cm^{-3}, and (c) 2.39 and 2.65 g cm^{-3}. Thick blue lines: locations of profiles presented in Figure 7.

The consistency of the two models along the southern shelf E-W BB′ is more questionable as *Bécel et al.* [2009] show a thinning under the limits of the İmralı basin, whereas our model gives a similar result as the profile under the NMT. However, the main data used to constrain this southern profile by *Bécel et al.* [2009] are shots along a MCS line, which was limited to the ship track east of Marmara Island. On the western extremity of this line, *Bécel* [2006] detected evidence of a deepening of the lower crust top and interpreted this as the edge of the thinning, concluding that the crust is unthinned under the Marmara Island. But the dip they detected could in fact correspond to the edge of the thinning centered, in our model, under the Çınarcık basin.

The third profile (CC′) interpreted by *Bécel et al.* [2009] is oriented NS and shows that a thinning under the North Marmara Trough is required in order to fit the computed *PmP* waves traveltime with records from the Oren on land station in the south. The profile in our model presents a shallower Moho overall, but the
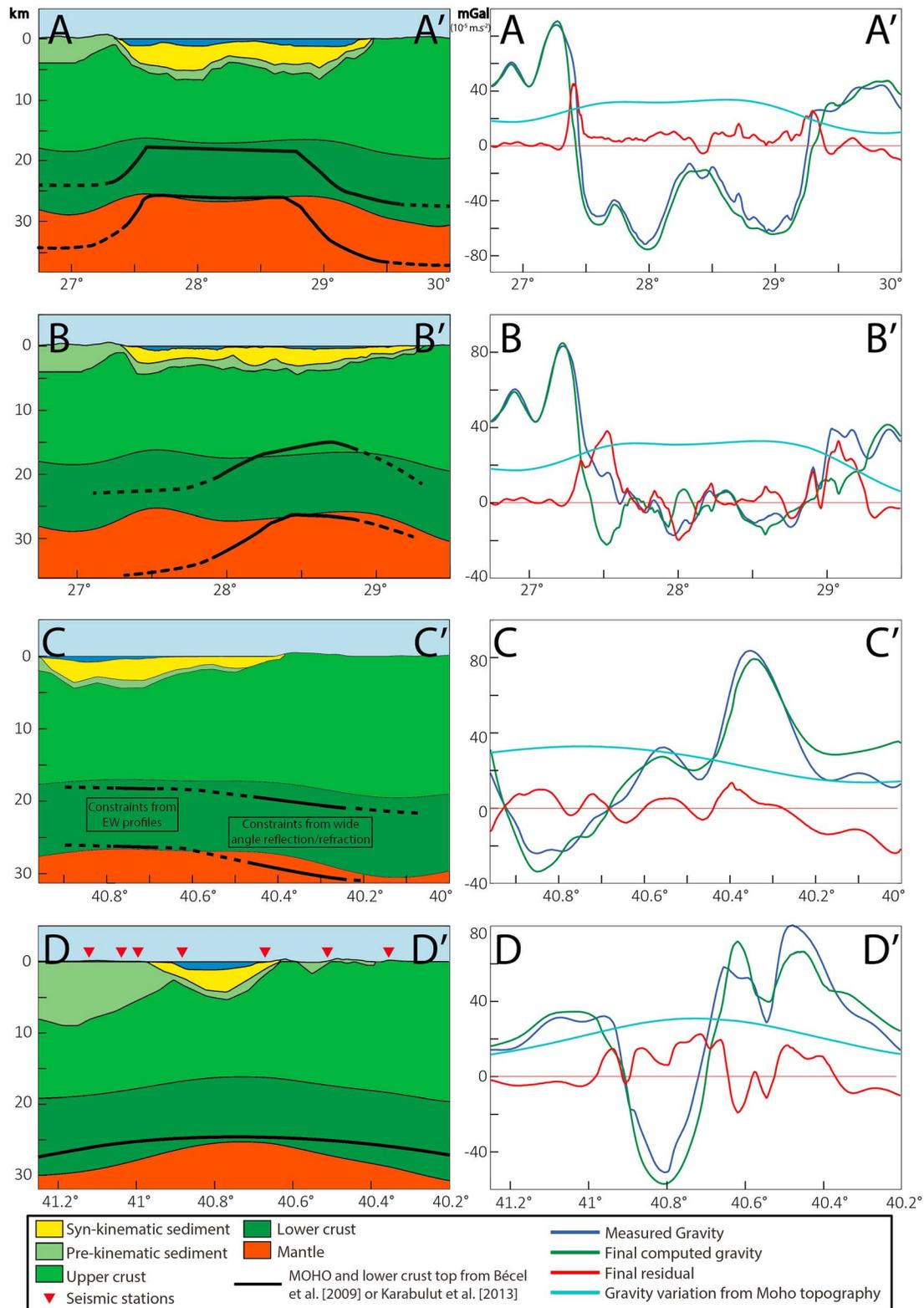
Figure 7. Gravity, geological data, and results along four profiles (see location in Figure 6a). (left column) Geological setting, modeled Moho, and modeled upper crust/lower crust boundary. (right column) Gravity measurement, computed gravity, residual anomaly, and gravity field induced by Moho depth variation. Profiles A, B, and C coincides with profiles presented in *Bécel et al.* [2009], and profiles D is localized in *Karabulut et al.* [2013] cross section. Bold black lines in Figure 7 (left column) represent *Bécel et al.* [2009] Moho and lower crust depth on profiles A, B, and C, and *Karabulut et al.* [2013] Moho depth on profile D. Dotted lines correspond to locations where seismic constraints are thin.
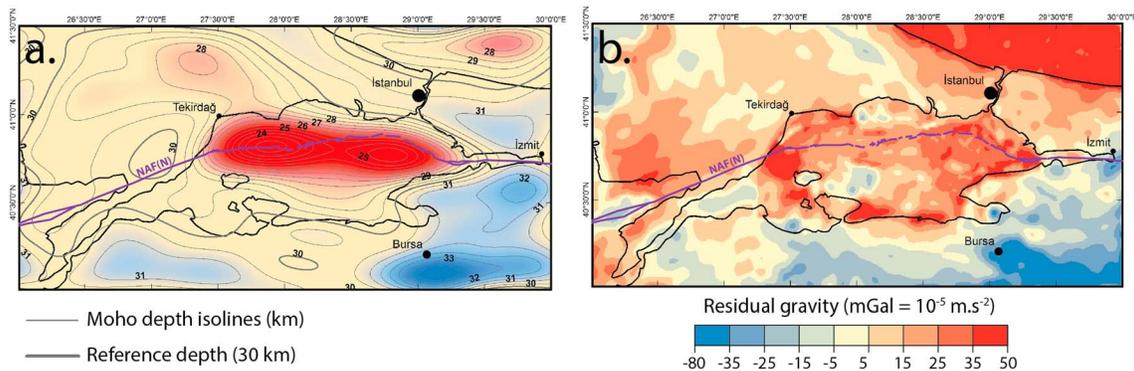
Figure 8. (a) Moho depth and (b) gravity residual of the isostatic model. Geological setting, gravity data, and sediment characteristics used as inputs are the same as in the previous models. The compensation depth is 35 km, and the reference crust thickness is 30 km The Moho topography is filtered to discard small wavelength. Apart from the filtering, it is a direct response to the geological model.

inclination inferred from the Oren station of 4.3° is very close to the inclination in our model, at the location of *Bécel et al.* [2009] constraint on the Moho.

To conclude, our model is consistent with *Bécel et al.* [2009] model where seismic data give good constraints. But unlike *Bécel et al.* [2009], who determined that the thinning is localized under the main basins, we propose that the thinning zone is wider and extends southward, including below the Marmara Island anticline [*Le Pichon et al.*, 2013].

The 650 km long profile presented in *Karabulut et al.* [2013] was constructed based on a tomography study using receiver functions. Because only on land stations were used, the data spacing is not tight in the Marmara Sea and there are gaps of about 65 km in the north and 30 km in the south between the stations along the shores and the next stations on the profile. As our model amplitude in profile DD′ was mainly based on *Karabulut et al.* [2013] study, we do observe the same depth in the middle of the Marmara Sea and away from the basins. However, the apparent wavelength of our model is different with a thinning spread on about 120 km compared to 220 km in *Karabulut et al.* [2013] model. Given that *Karabulut et al.* [2013] horizontal resolution is about 40 km, the two models are not inconsistent.

4.2. Isostatic Model

To evaluate further the validity of our model, we compared it to an isostatic filtered model. The isostatic Moho model was calculated through an Airy mass compensation condition on columns of 35 km thickness and of about 0.4 km^2. The compensation was made to fit with an ideal column of 30 km of crust and 5 km of mantle. The basin model is the same as before, with two sediments layers. The resulting Moho was filtered through a Butterworth low-pass filter set to give the best correlation coefficient of the two models frequency signatures.

The result (see Figure 8b) is close to the Moho inverted from gravity values, with two areas of maximum thinning in the eastern and western parts of the Sea of Marmara. Also, the western zone of thinning in the isostatic model is centered NE of the Marmara Island, not north of the island. This result is unsurprising as, by construction, the isostatically compensated Moho image is merely a filtered image of the basin geometry. The maximum thinning zones thus correspond to the areas with the highest thicknesses of basin fill. The range of Moho depth variations is also comparable, which indicates that the present-day basin geometry is in large part isostatically compensated. However, local comparison with our model indicates that there is an isostatic deficit under the NMT but an excessive compensation under the southern basins where our modeled Moho is higher than the isostatic Moho.

The residual gravity anomaly (difference between measured gravity and modeled gravity anomaly) is significantly larger with the isostatic model than with the inversion results. This is because the Moho uplift in the isostatic model is too narrow to create a prominent gravity variation. Thus, the small amplitude of the gravity anomaly generated by the isostatic Moho uplift cannot compensate for the gravity anomaly in the Marmara Sea after basin correction (see Figure 5). As the amplitude of the gravity anomalies are filtered

depending on wavelength and interface depth, according to equation (2), the Moho uplift would need to have a larger amplitude or to contain longer wavelengths in order to fit the gravity anomaly. A larger amplitude is not very realistic as it would imply that there is a net mass excess where the basins are deeper. But longer wavelengths are what our model suggests. In any case, a model based solely on local isostasy cannot explain the gravity anomaly.

4.3. Uncertainties

The main factor that may compromise the accuracy of the Moho topography and of the various calculations based on it is that we did not considered laterally variable densities. As illustrated by *Aydin et al.* [2005], below the Sea of Marmara and south of it, Curie-point depths are higher than 20 km. As a consequence, higher temperatures and lower densities in the lower crust and in the mantle are expected. This may not be problematic for the application of the Parker method as density variations at interface should not fluctuate significantly, but a thermal gravity correction could deal with gravity anomalies generated by lower densities [*Bai et al.*, 2014]. Since the temperature variations is oriented NS, such a correction would lower the visible divergence in the gravity anomaly before inversion (see Figure 5) between the north and the south. However, the amplitude of this anomaly is small compared to the anomalies dominating the Marmara Sea area. Only a small impact in the final result is expected. If this anomaly was corrected before inversion, we would predict a deeper Moho in the north and a relatively higher Moho in the south. This could in part explain the apparently thinner crust in our model beneath the Istanbul block, which appears as a relatively cold zone in the Curie-point map [*Aydin et al.*, 2005].

Furthermore, we defined our sediment and upper crust limits from density and/or age contrasts, regardless of rock types. If this model is well constrained in the Marmara Sea from the seismic data, uncertainties increase away from the sea. This effect adds up to the fact that the upper/lower crust density contrast is also solely constrained in the Marmara Sea by *Bécel et al.* [2009] deep surveys. However, the data coverage is sufficient to rule out the isostatically compensated model in which the Moho uplift would be mostly confined below the deep basins.

Another source of uncertainty is the likely existence of a damage zone with low *P* wave and *S* wave velocity and low density along the Main Marmara Fault. Since data sets in the Marmara Sea still lack a fine enough resolution to reveal the geometry and characteristics of such a zone, we did not integrate it in our model but used the characteristics of the San Andreas Fault low-velocity zone to evaluate the impact that such a zone could have on the Moho model in the Marmara Sea. Recent studies based on the San Andreas Fault Observatory at Depth project have shown that the damaged zone is about 200 m and extends at least as deep as 7 km [*Jeppson and Tobin*, 2015; *Li and Malin*, 2008]. We used the 2-D equation by *Telford et al.* [1990] for calculating the 2-D gravity effect of a vertical dyke (applied to a zone of low density along a fault). We considered a 200 to 300 m wide zone reaching the surface and going as deep as 15 km, which corresponds to the maximum depth of the brittle crust floor [*Schmittbuhl et al.*, 2016]. We evaluated the maximum value of the density anomaly to 400 kg/m^3 using velocity-density relationships proposed for the San Andreas Fault damage zone [*Roecker et al.*, 2004]. We thus obtain a maximum anomaly accounting for the density loss along the fault of −8.9 mGal, which drops to −1.8 mGal 5 km away from the fault. As for the impact on the Moho modeling, the uplift of the Moho found after correcting for the effect of a damaged zone is increased by a maximum of 120 m under the fault, which has a negligible effect on the volume calculations we will carry in the discussion.

5. Discussion

The Moho depth variation model computed in this study shows a distribution of thinning which appears to roughly mimic the base of the syntectonic basins [*Bayrakci et al.*, 2013]. The Moho highs do not exactly match the upper crust lows but are both close to the two Marmara most active basins. The two highs are separated by an inflection in the Moho roughly at the Central High location, where the minimum extension is observed in the North Marmara Trough. The thinning also appears to spread over a wider zone. This indicates that the stretching component of strain in the Marmara Sea has been distributed differently in the upper crust and at the Moho level, implying some ductile flows in the lower crust.

If this model is hardly compatible with any model based on rigid blocks, like *Armijo et al.* [1999] block model based on present-day active fault geometry in the brittle crust, it shows a geometric compatibility with the
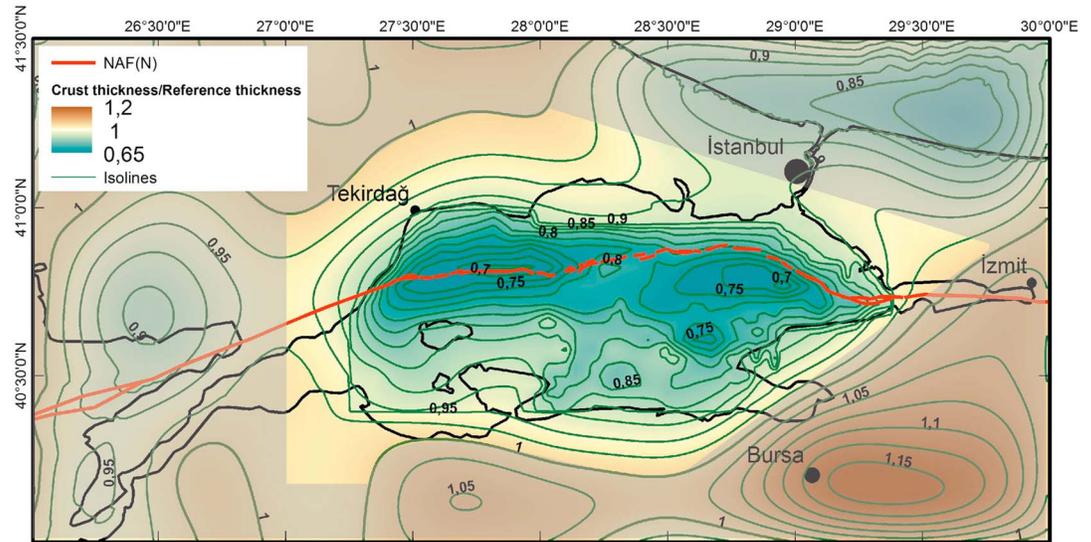
Figure 9. Thinning rate corresponding to our model crust thickness over 30 km reference thickness. The unshaded area correspond to the zone that was considered in a crust volume calculation to estimate a 2100 ± 250 km^2 extension surface in the Marmara Sea.

low-angle detachment system identified in the Eastern and Central Marmara Sea from seismic reflection and refraction profiles [*Bécel et al.*, 2010]. But the zone of crustal thinning still appears broader extending below the southern shelf and the Marmara Island. A more detailed comparison of the Moho topography and of the basement topography is presented in *Le Pichon et al.* [2015].

5.1. Overall Extension in the Marmara Sea

To quantify the overall extension accommodated during the Marmara Sea basins formation, we considered the volume difference between the crust in our model and a reference prekinematic model with a constant 30 km thick crust and no sediment basins nor hills. Here, the term "crust," refers to the lower and upper crust, as well as to the prekinematic sediment. In order to avoid interferences from older geological systems, we discarded zones where the Moho depth variations are influenced by pre-Pliocene tectonics, for instance, the Uludağ massif which exhumation occurred during the early Miocene [*Okay et al.*, 2008], the Black Sea, and the Thrace basin. Figure 9 shows the final 19450 km^2 area we considered.

We computed the proportion of the area that could be accommodated with this ideal crust, given the volume of crust in our model. We obtained that, with the volume of crust given by our model in the 19450 km^2 area we defined, a 30 km thick reference crust could cover only 17400 ± 300 km^2. Thus, our model indicates a total of 2050 ± 300 km^2 of extension during the formation of the Marmara Sea. Figure 10 shows a schematic explanation of this calculation. The uncertainty is obtained by varying the sediment densities within the defined
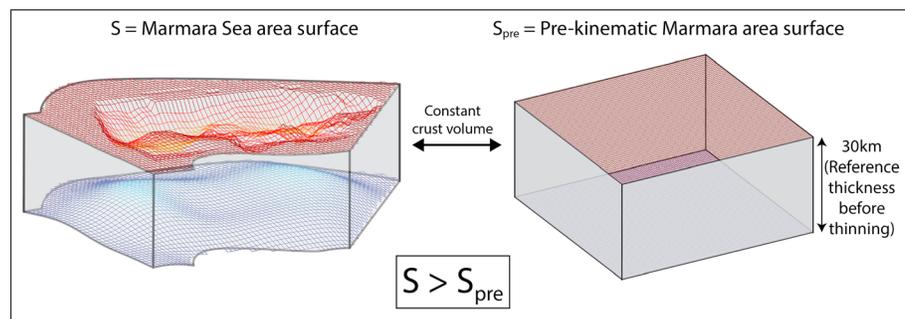
Figure 10. Schematic explanation of the extension surface calculation. The surface difference between the current model and the ideal prekinematic model corresponds to the extension. We compute the prekinematic block surface regardless of its shape.

bounds and varying the reference Moho depth by 2 km around the 30 km reference value, which corresponds to *Karabulut et al.* [2013] estimated uncertainty on Moho picks. Because the reference thickness is also an input for the Moho topography inversion, the uncertainty on "missing" surface may seem smaller than expected.

Armijo et al. [2002] presented a reconstitution of the area at −5 Myr based on present-day active fault geometry in the brittle crust. They delimited four rigid blocks creating two main zones where oblique slip and extension occur, along the deep basins and along the southern coast. A third zone, farther south, will not be considered as it is in great part outside of the area we modeled. Between these two systems, an additional fault system identified beneath the southern continental shelf, the Southern Marmara Fault, has been mostly active during the Pliocene [*Le Pichon et al.*, 2013]. The total slip on the shelf fault is not precisely known, and this fault was interpreted as a dominantly transpressional, deformation with only local transtension associated with fault bends. A reconstitution assuming an offset of 85 km on the Ganos fault branch [*Armijo et al.*, 2002] yields a surface increase by extension of about 6900 km^2 with, respectively, 3200 km^2 and 3700 km^2 along the deep basins and the southern shelf. This is about 3 times the value we found. Matching those results would imply an average initial crust thickness of 42 km. Other parameters are displacement and slip obliquity. It is possible that the block model overestimates obliquity. Reducing obliquity in the Marmara Sea would increase compression generated at the fault bends in Ganos Mountain area in the west and Armutlu area in the east. This compression today results in active uplift but did not result in an observable crustal thickening yet. We conclude that reducing the obliquity is unlikely to solve the discrepancy. More likely, the total 85 km slip assumed in the block model is an overestimate. The thinned domain that we obtain from gravity modeling appears wider than the Marmara Trough and extends southward beneath the shelf, but is not resolved as two distinct zones of extension. The distribution of crustal thickness thus obtained does not support the presence of a large component of localized extension along the southern fault system. Although the presence of active fault scarps running along the Southern Marmara coast between Gemlik Bay and Kapıdağ Peninsula can be argued based on geomorphology, the eastward connection of this fault system to Ganos fault is unclear. A southwestward prolongation and connection with the southern branch of the NAF are another possibility [e.g., *Şengör et al.*, 2014] that would produce less extension and also less displacement along Ganos fault. It is thus possible that the total extension across the Southern Marmara zone is much smaller than in the block model of *Armijo et al.* [2002]. In fact, in the block model, the extension in the northern zone alone is a better match for the extension we calculated over the whole Marmara Sea area.

In this total surface extension calculation, we used the reference 30 km depth as the thickness of the crust before deformation. However, in this area where the Hellenic subduction rollback has been active for more than 20 Myr [*Jolivet and Faccenna*, 2000], it is possible that a large-scale thinning and smoothing by ductile flow in the lower crust have occurred, even though we do observe 30 km as the average value in the region around the Marmara Sea [*Karabulut et al.*, 2013; *Tiberi et al.*, 2001]. In that case, the construction of the Moho variation with regards of a local reference depth would still be valid, but a more regional reference depth should be considered in the calculation of overall extension.

5.2. Tectonic Regime Evolution During the Last 5 Myr

A complementary approach is to compare our estimate of finite extension with estimated present-day rate of extension from geodesy. Geodetic data cannot constrain the distribution of motion within the Marmara Sea, but the bulk extension of the domain comprised within the same area as the one we selected (see Figure 9) may be calculated from interpolated velocity fields [*Özeren and Holt*, 2010]. The deformation field in the Marmara Sea area was calculated based on a new mathematical approach based on solving for the elastic deformation sources [*Haines et al.*, 2015]. In zones, like the Marmara Sea, which have dense GPS data along the boundaries of the domain of interest, this approach provides an interpolation of the deformation field within the domain consistent with an assumption of elastic strain in a homogeneous upper crust. However, results are independent of assumptions on where faults are located and thus cannot be used to ascertain slip rates on offshore faults. The areal strain is calculated from the divergence of the vertical derivatives of horizontal stress (VDoHS) rates, divided by an elastic constant, and is equal to the divergence of the velocity field. Using the GPS data presented in *Reilinger et al.* [2006], we calculated the extension rate in our domain by considering the areal strain integrated over a wide zone covering the entire thinned crust domain. This result does not depend on the details of the VDoHS field. We obtained an extension rate on our surface of 396 km^2 Myr^{-1}.

Thus, considering the total finite extension calculated before and assuming a stable extension rate similar to the present rate, the Marmara Sea extension could have been formed in 5.2 ± 0.7 Myr. Although this time period could have accommodated a stable extension rate, there is little chance that the fault system and the way the extension was distributed has been steady as 5 Myr is considered as the maximal age for the incursion of the North Anatolian Fault system in the Marmara Sea [*Şengör et al.*, 2005; *Armijo et al.*, 1999]. In fact, variations with time of the rate, the width of the deformation zone, and of the rate of motion are suspected [e.g., *Şengör et al.*, 2005]. *Grall et al.* [2012] identified a progressive change in basin subsidence distribution in the Marmara Central Basin, implying that the zone affected by extension has been wider during some time in the Pliocene, likely in relation with detachment systems identified in seismic reflection data [*Bécel et al.*, 2009]. *Le Pichon et al.* [2015] propose that a system analogous to the Corinth detachment system was active in the Pliocene between 4.5 and 3.5 Myr, prior to the initiation of the Main Marmara Fault, and accommodated strain at the tip of the propagating North Anatolian Fault. The beginning of this extension phase as described by *Le Pichon et al.* [2015] lies in the uncertainty range of our evaluation based on present-day extension rate and Moho topography. We propose that the extension strain in the Marmara zone has been stable or slightly decreasing since the Pliocene, maintaining a constant overall regional extension, but that the incursion of the North Anatolian Fault system restructured the distribution of the extension from a wide zone with high-scale detachment and distributed extension to the current situation where extension is mostly carried along the Main Marmara Fault.

For the last 1.5 Myr, considering a geological slip rate of 18 mm/yr on the Main Marmara Fault [*Le Pichon et al.*, 2015; *Grall et al.*, 2013; *Kurt et al.*, 2013] and supposing that the extension was evenly carried along the 160 km long North Marmara Trough, our surface extension rate leads to an extension rate of 2.5 mm/yr and an average angular obliquity of 7.9° between velocity vector and local plate boundary orientation.

Based on the repartition of the crust thinning (see Figure 9), we can make a few assumptions on how the purely extensive system was functioning prior to the North Anatolian Fault propagation. We see that there is a striking difference between two zones, delimited approximately by a SW-NE line crossing the eastern tip of the Kapıdağ Peninsula and the Kumburgaz basin. In the eastern zone, the thinning is stretched all the way to the southern coast line where the crust thickness is only 80% of our reference thickness. In the western zone, only a small zone centered on the Tekirdağ basin southern limit shows a crust thickness below 80% of our reference thickness, and the Main Marmara Fault crosses the zone at the maximum of the thinned zone. In the east, the shifting of the fault in respect of the thinned zone could simply be the effect of the Çınarcık basin fast subsidence [*Le Pichon et al.*, 2015], originating from the releasing bend [*Kurt et al.*, 2013]. On the other hand, in the west, there is no shifting of the thinning toward the Tekirdağ basin depocenter. We explain this dissimilarity by a difference in the setting before the fault propagation. In the west, where evidence of a large-scale detachment is yet to be found, the extension may have been distributed on multiple fault zones. Thus, no well-defined zone of thinning was created. Whereas in the east, detachment functioning [*Bécel et al.*, 2009; *Le Pichon et al.*, 2015] caused a broad but well-defined thinned zone. In this zone, the lower crust was weakened by isotherm rising and ductile flows were facilitated. After the propagation of the North Anatolian Fault northern branch, the extension was mostly carried by asymmetrical basins along the main fault. However, in the eastern Marmara zone the extension system remained active, as indicated by steady state subsidence in İmralı basin [*Sorlien et al.*, 2012], and facilitated the equalization and the spreading of the Moho indentation by ductile flow from the south, maintaining a shift of the thinning location toward the south of the fault. In the following part, we quantify the ductile flow in the lower crust.

5.3. Upper and Lower Crust Extension Budget and Ductile Flow in the Lower Crust

If stretching is independent of depth, as in *McKenzie* [1978] model, and if local isostatic compensation is applied at the Moho, the indentation of the Moho should nearly be a mirror image of the basin geometry. The results of the gravity inversion indicate that this is not the case in the Sea of Marmara, and we argued that ductile flow in the lower crust could be at least part of the explanation. In the following we will show that the volume of lower crustal flow does not need to be large to explain the observations.

Let us divide the thinned crust area along latitude 40.7°N into a northern domain containing the Northern Marmara Troughs and a southern domain (see Figure 11). We assume that the volume of the basins and of the Moho uplift is proportional to the stretching taking place in the upper crust and in the lower crust, respectively. We also assume that ductile flow in the lower crust fully accounts for discrepancies in the stretching
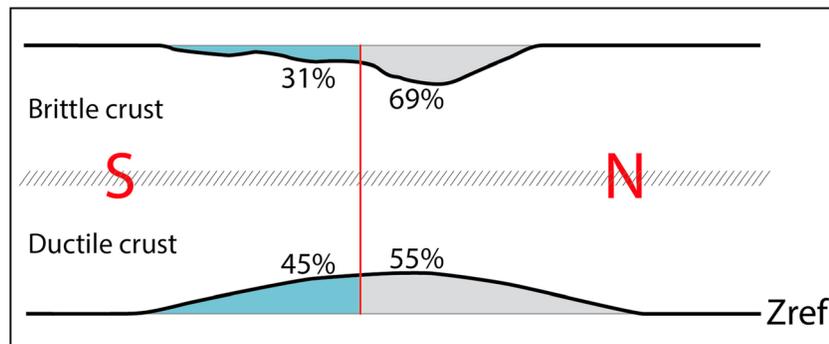
Figure 11. Schematic 2-D illustration of the comparison between the basin volume in the upper crust and the Moho uplift in the lower crust. Considering that these volumes are proxies for the stretching and that lower crust thinning that is not proportionally observed in the upper crust implies ductile flow, we find that 14% of the uplift in the lower crust is shifted from the northern block (N) to the southern block (S) and is related to lateral ductile flow.

distribution between the upper crust and the lower crust. Thus, comparing the distribution of the basin volume and of the Moho indentation in each domain will give us a maximum value for ductile flow between the northern and the southern domain. Our model indicates that, in the upper crust, 69% of the basin volume is in the northern domain while the rest, 31%, is in the south. In the lower crust, only 55% of the Moho uplift is in the northern domain and 45% is in the southern domain (see Figure 11). We conclude that 14% of the Moho uplift volume is moved between the northern and southern domain, compared with the case where the distribution of extension is the same in the upper and lower crust (69% versus 31%). This corresponds to 5.8×10^{12} m^3 of crust material that was displaced northward to accommodate for the Moho uplift. Considering that this volume is a maximization of the ductile flow in the lower crust, the maximum surface extension related to the ductile flow can be calculated knowing the ductile crust thickness.

Microseismicity distribution indicates that the floor of the brittle crust is at around 15 km [*Schmittbuhl et al.*, 2016]. However, some lateral variations of the brittle crust thickness can be suspected as the geothermal gradient increases from north to south of the Marmara Sea. *Aydin et al.* [2005] indicates that the Curie-point depth reaches about 24 km within Istanbul block in the north and decreases to about 12 km south of the Marmara Sea. Regional magnetic studies find an average Curie-point depth of 14.5 km in the Marmara Sea area, compatible with seismicity depth distribution [*Ates et al.*, 2003], but the resolution of the spectral method used in both studies is insufficient to resolve the details of the north-south Curie-point gradient at the local scale. In addition, the maximum depth at which the upper crustal detachments could be imaged in the Eastern Marmara Sea is 13 km [*Bécel et al.*, 2009]. We thus retain a brittle crust thickness of about 15 km, possibly thinner in extended domains. This corresponds to an initial ductile lower crust thickness of about 15 km.

We estimated earlier that the maximum volume of lower crust flow transferred from the southern to the northern domain to account for the lateral variation of lower crustal thickness compared to upper crustal thickness is 5.8×10^{12} m^3. The average surface of lower crust transferred is thus 390 to 585 km^2, assuming that the thickness of the ductile layer is in the 10–15 km range. This represents about 15–30% of the total 2050 ± 300 km^2 surface extension during the Marmara Sea basin formation. Considering that the length of the Marmara Sea is 160 km, out of 12.8 ± 1.9 km of extension perpendicular to the E-W direction of the Main Marmara Fault, the shearing between upper and lower crust needed to explain the distribution of crustal thickness only amounts to 2.4 to 3.7 km. Even if our model is quite schematic and maximizes ductile flow in the lower crust, this maximum flow is relatively small compared to the total extension. This shows that moderate upper/lower crust decoupling can account for the observed distribution of extension in the upper and lower crust.

In fact, with a brittle crust thickness of about 15 km and a maximum sediment thickness of about 6 km, the Marmara Sea case fits *Petrunin and Sobolev* [2006] results of rheological models linking brittle crust thickness and sediment thickness, intermediate between the Gulf of Aqaba and the Dead Sea cases considered in their study. Some involvement of the lower crust is thus probably needed to account for the Moho uplift under the Marmara Sea as well as for the southward spread of the extended domain. Unlike under the Dead Sea, the

crust is ductile enough for a partial compensation within the crust and some Moho uplift to occur but, unlike under the Death Valley, ductile flows are not sufficient to regionally flatten the Moho. Whether the Marmara Sea is more representative of strike-slip basins in continental crust worldwide cannot be assessed easily as cases with well-constrained Moho geometry are relatively few. Several other well-studied cases correspond to older basins with complex history [e.g., Songliao basin; *Wang et al.*, 2007; *Liu and Niu*, 2011] or to active basins with more advanced extension (e.g., Andaman Sea [*Morley and Alvey*, 2015]). Moreover, the tectonics of the Marmara Sea are influenced by the interaction between the NAF strike-slip system and the Western Anatolian extension driven by the Aegean subduction [*Le Pichon et al.*, 2015]. We also noted a difference in the geothermal gradient north and south of the Marmara Sea [*Aydin et al.*, 2005]. The combination of these factors may have favored the development of crustal extension south of the present location of the main strike-slip fault.

6. Conclusion

Using the Parker method and a new inversion method we developed for this study, we corrected the free-air gravity anomaly in the Marmara area from the topography and density structure of the sedimentary basins and built a Moho depth model showing a saddle shaped uplift under the Marmara Sea. From a reference depth of 30 km, the Moho shows two main uplifts reaching over 25 km, centered north of the Marmara Island and below the İmralı and Çınarcık basins, and connected by a ridge staying above 27 km. The main novel contribution of this model is to show that the thinning is not limited to the NMT but extends farther than the Marmara Sea coasts. While this finding is consistent with the hypothesis of an early phase of extension involving crustal-scale detachments [*Bécel et al.*, 2009; *Le Pichon et al.*, 2015], we propose that this early stage process is associated with a steady state lower crustal flow toward the deep Marmara Trough in a continuously evolving fault system. The gravity residual after correcting for the whole basin and crust model shows that there is no remaining large wavelength anomalies which, together with the 1 km average Moho depth error, testifies for our model robustness.

The Moho topography map and the upper crust model constitute a 3-D model of the crust. The comparison of this model with an ideal unthinned crust of the same volume gave us the total surface extension during the formation of the Marmara Sea basins. We found 2050 ± 300 km^2, corresponding to 12.8 ± 1.9 km of extension in a direction normal to the plate boundary along the 160 km long Marmara Sea. When related to the current GPS-derived areal extension rate of 396 km^2 Myr^{-1}, it leads to an age of 5.2 ± 0.7 Myr for the system. This age span is roughly compatible with the geological age of the Marmara Sea basins

The difference in the apparent distribution of extension at the upper crustal level, from basin geometry, and at the Moho level, from the gravity inversion, may be explained by minor decoupling between upper and lower crust deformation. A horizontal displacement in the lower crust of about 3 km toward the north (representing about 25% of the total extension and less than 6% of the total motion accommodated in the Marmara Sea strike-slip zone) can explain the amplitude of the Moho uplift south of the NMT. However, the relative contribution to the present-day crustal structure of ductile lower crust deformation and early extension before the incursion of the North Anatolian Fault still needs to be assessed.

Finally, we propose that the Marmara Sea lower crust ductility is intermediate between the two much studied end-member cases of transform extension zone, the Dead Sea and the Death Valley, where no Moho uplift is observed. Moho uplift can be interpreted primarily as a consequence of crustal rheology, but the boundary conditions (Aegean extension in the Marmara Sea case) can also influence the amount and distribution of crustal extension and should be taken into account when comparing with other strike-slip basins worldwide.

References

Aitken, A. R. A., M. L. Salmon, and B. L. N. Kennett (2013), Australia's Moho: A test of the usefulness of gravity modelling for the determination of Moho depth, *Tectonophysics*, *609*, 468–479, doi:10.1016/j.tecto.2012.06.049.

Aloisi, G., G. Soulet, P. Henry, K. Wallmann, R. Sauvestre, C. Vallet-Coulomb, C. Lécuyer, and E. Bard (2015), Freshening of the Marmara Sea prior to its post-glacial reconnection to the Mediterranean Sea, *Earth Planet. Sci. Lett.*, *413*, 176–185, doi:10.1016/j.epsl.2014.12.052.

Armijo, R., B. Meyer, A. Hubert, and A. Barka (1999), Westward propagation of the North Anatolian fault into the northern Aegean: Timing and kinematics, *Geology*, doi:10.1130/0091-7613(1999)027<0267:WPOTNA>2.3.CO;2.

Armijo, R., B. Meyer, S. Navarro, G. King, and A. Barka (2002), Asymmetric slip partitioning in the Sea of Marmara pull-apart: A clue to propagation processes of the North Anatolian Fault?, *Terra Nova*, *14*(2), 80–86, doi:10.1046/j.1365-3121.2002.00397.x.

Ates, A., T. Kayıran, and I. Sincer (2003), Structural interpretation of the Marmara region, NW Turkey, from aeromagnetic, seismic and gravity data, *Tectonophysics*, *367*, 41–99, doi:10.1016/S0040-1951(03)00044-1.

Aydin, I., H. I. Karat, and A. Koçak (2005), Curie-point depth map of Turkey, *Geophys. J. Int.*, *162*, 633–640, doi:10.1111/j.1365-246X.2005.02617.x.

Bai, Y., S. E. Williams, R. D. Müller, Z. Liu, and M. Hosseinpour (2014), Mapping crustal thickness using marine gravity data: Methods and uncertainties, *Geophysics*, *79*(2), G27–G36, doi:10.1190/geo2013-0270.1.

Bayrakci, G., M. Laigle, A. Bécel, A. Hirn, T. Taymaz, S. Yolsal-Cevikbilen, and S. Team (2013), 3-D sediment-basement tomography of the northern Marmara trough by a dense OBS network at the nodes of a grid of controlled source profiles along the North Anatolian fault, *Geophys. J. Int.*, *194*(3), 1335–1357, doi:10.1093/gji/ggt211.

Bécel, A. (2006), Structure Sismique de la Faille Nord Anatolienne en Mer de Marmara, Phd Thesis, Institut de Physique du Globe de Paris.

Bécel, A., et al. (2009), Moho, crustal architecture and deep deformation under the north Marmara Trough, from the SEISMARMARA Leg 1 offshore-onshore reflection-refraction survey, *Tectonophysics*, *467*(1-4), 1–21, doi:10.1016/j.tecto.2008.10.022.

Bécel, A., M. Laigle, B. de Voogd, A. Hirn, T. Taymaz, S. Yolsal-Cevikbilen, and H. Shimamura (2010), North Marmara Trough architecture of basin infill, basement and faults, from PSDM reflection and OBS refraction seismics, *Tectonophysics*, *490*(1-2), 1–14, doi:10.1016/j.tecto.2010.04.004.

Ben-avraham, Z., R. Hänel, and H. Villinger (1978), Heat flow through the Dead Sea rift, *Mar. Geol.*, *28*, 253–269, doi:10.1016/0025-3227(78)90021-X.

Ben-Zion, Y., Z. Peng, D. Okaya, L. Seeber, J. G. Armbruster, N. Ozer, A. J. Michael, S. Baris, and M. Aktar (2003), A shallow fault-zone structure illuminated by trapped waves in the Karadere-Duzce branch of the North Anatolian Fault, western Turkey, *Geophys. J. Int.*, *152*, 699–717.

Biddle, K. T., and N. Christie-Blick (1985), Glossary—Strike-slip deformation, basin formation, and sedimentation, *Spec. Publ. Soc. Econ. Paleontol. Mineral.*, 375–386.

Burchfiel, B. C., and J. H. Stewart (1966), "Pull-apart" origin of the central segment of Death Valley, California, *Geol. Soc. Am. Bull.*, *77*(April 1966), 439–442, doi:10.1130/0016-7606.

Christensen, N. I., and W. D. Mooney (1995), Seismic velocity structure and composition of the continental crust: A global view, *J. Geophys. Res.*, *100*(B6), 9761–9788, doi:10.1029/95JB00259.

Christie-Blick, N., and K. T. Biddle (1985), Deformation and basin formation along strike-slip faults, *Soc. Sediment. Geol.*, *37*, 1–34, doi:10.2110/pec.85.37.0001.

De Voogd, B., L. Serpa, and L. Brown (1988), Crustal extension and magmatic processes: COCORP profiles from Death Valley and the Rio Grande rift, *Geol. Soc. Am. Bull.*, *100*, 1550–1567, doi:10.1130/0016-7606(1988)100<1550:CEAMPC>2.3.CO;2.

Erickson, S. N., and Jarrard, R. D. (1998), Velocity-porosity relationships for water-saturated siliciclastic sediments, *J. Geophys. Res.*, *103*, 30,385–-30,406, doi:10.1029/98JB02128.

Feng, R., and T. V. McEvilly (1983), Interpretation of seismic reflection profiling data for the structure of the San Andreas Fault zone, *Bull. Seismol. Soc. Am.*, *73*(6A), 1701–1720.

Fliedner, M. M., et al. (1996), Three-dimensional crustal structure of the southern Sierra Nevada from seismic fan profiles and gravity modeling, *Geology*, *24*(4), 367–370, doi:10.1130/0091-7613(1996)024<0367:TDCSOT>2.3.CO;2.

Garfunkel, Z., and Z. Ben-Avraham (1996), The structure of the Dead Sea basin, *Tectonophysics*, *266*(1), 155–176, doi:10.1016/S0040-1951(96)00188-6.

Gómez-Ortiz, D., and B. N. P. Agarwal (2005), 3DINVER.M: A MATLAB program to invert the gravity anomaly over a 3-D horizontal density interface by Parker-Oldenburg's algorithm, *C. R. Geosci.*, *31*(4), 513–520, doi:10.1016/j.cageo.2004.11.004.

Grall, C., P. Henry, D. Tezcan, B. Mercier de Lepinay, A. Bécel, L. Geli, J.-L. Rudkiewicz, T. Zitter, and F. Harmegnies (2012), Heat flow in the Sea of Marmara Central Basin: Possible implications for the tectonic evolution of the North Anatolian fault, *Geology*, *40*(1), 3–6, doi:10.1130/G32192.1.

Grall, C., P. Henry, Y. Thomas, G. Westbrook, M. Cagatay, B. Marsset, H. Saritas, G. Çifçi, and L. Géli (2013), Slip rate estimation along the western segment of the Main Marmara 1 Fault over the last 405-490 ka by correlating mass transport deposits, *Tectonics*, *32*, 1587–1601, doi:10.1002/2012TC003255.

Haines, A. J., L. L. Dimitrova, L. M. Wallace, and C. A. Williams (2015), *Enhanced Surface Imaging of Crustal Deformation: Obtaining Tectonic Force Fields Using GPS Data*, Springer, Cham.

Hergert, T., and O. Heidbach (2010), Slip-rate variability and distributed deformation in the Marmara Sea fault system, *Nat. Geosci.*, *3*(2), 132–135, doi:10.1038/ngeo739.

Huvaz, O., N. Karahanoglu, and V. Ediger (2007), The thermal gradient of the Thrace basin, NW Turkey: Correlation with basin evolution processes, *J. Pet. Geol.*, *30*(1), 3–24, doi:10.1111/j.1747-5457.2007.00003.x.

Jeppson, T. N., and H. J. Tobin (2015), San Andreas Fault zone velocity structure at SAFOD at core, log, and seismic scales, *J. Geophys. Res. Solid Earth*, *120*, 4983–4997, doi:10.1002/2015JB012043.

Jolivet, L., and C. Faccenna (2000), Mediterranean extension and the Africa-Eurasia collision, *Tectonics*, *19*(6), 1095–1106, doi:10.1029/2000TC900018.

Karabulut, H., A. Paul, T. Afacan Ergun, D. Hatzfeld, D. M. Childs, and M. Aktar (2013), Long-wavelength undulations of the seismic Moho beneath the strongly stretched western Anatolia, *Geophys. J. Int.*, *194*(1), 450–464, doi:10.1093/gji/ggt100.

Katzman, R., U. S. Ten Brink, and J. Lin (1995), Three-dimensional modeling of pull-apart basins: Implications for the tectonics of the Dead Sea basin, *J. Geophys. Res.*, *100*(B4), 6295–6312, doi:10.1029/94JB03101.

Kurt, H., et al. (2013), Steady late quaternary slip rate on the Cinarcik section of the North Anatolian Fault near Istanbul, Turkey, *Geophys. Res. Lett.*, *40*, 4555–4559, doi:10.1002/grl.50882.

Laigle, M., A. Bécel, B. de Voogd, A. Hirn, T. Taymaz, and S. Ozalaybey (2008), A first deep seismic survey in the Sea of Marmara: Deep basins and whole crust architecture and evolution, *Earth Planet. Sci. Lett.*, *270*(3-4), 168–179, doi:10.1016/j.epsl.2008.02.031.

Le Pichon, X., P. Henry, and S. Lallemant (1990), Water flow in the Barbados Accretionary Complex, *J. Geophys. Res.*, *95*(B6), 8945–8967, doi:10.1029/JB095iB06p08945.

Le Pichon, X., R. Saatc, and B. Tok (2001), The active Main Marmara Fault, *Earth Planet. Sci. Lett.*, *192*, 595–616.

Le Pichon, X., C. İmren, C. Rangin, A. M. C. Şengör, and M. Siyako (2013), The south Marmara Fault, *Int. J. Earth Sci.*, *103*(1), 219–231, doi:10.1007/s00531-013-0950-0.

Le Pichon, X., A. M. C. Şengör, J. Kende, C. İmren, P. Henry, C. Grall, and H. Karabulut (2015), Propagation of a strike-slip plate boundary within an extensional environment: The westward propagation of the North Anatolian Fault, *Can. J. Earth Sci.*, *53*, doi:10.1139/cjes-2015-0129.

Li, Y.-G., and P. E. Malin (2008), San Andreas Fault damage at SAFOD viewed with fault-guided waves, *Geophys. Res. Lett.*, *35*, L08304, doi:10.1029/2007GL032924.

Liu, H., and F. Niu (2011), Receiver function study of the crustal structure of Northeast China: Seismic evidence for a mantle upwelling beneath the eastern flank of the Songliao basin and the Changbaishan region, *Earthq. Sci.*, *24*(1), 27–33, doi:10.1007/s11589-011-0766-6.

McKenzie, D. (1978), Some remarks on the development of sedimentary basins, *Earth Planet. Sci. Lett.*, *40*(1), 25–32, doi:10.1016/0012-821X(78)90071-7.

Morley, C. K., and A. Alvey (2015), Is spreading prolonged, episodic or incipient in the Andaman Sea? Evidence from deepwater sedimentation, *J. Asian Earth Sci.*, *98*, 446–456, doi:10.1016/j.jseaes.2014.11.033.

Okay, A. I., M. Satir, M. Zattin, W. Cavazza, and G. Topuz (2008), An Oligocene ductile strike-slip shear zone: The Uludag massif, northwest Turkey—Implications for the westward translation of Anatolia, *Geol. Soc. Am. Bull.*, *120*(7-8), 893–911, doi:10.1130/B26229.1.

Oldenburg, D. W. (1974), The inversion and interpretation of gravity anomalies, *Geophysics*, *39*(4), 526–536.

Özeren, M. S., and W. E. Holt (2010), The dynamics of the eastern Mediterranean and eastern Turkey, *Geophys. J. Int.*, *183*(3), 1165–1184, doi:10.1111/j.1365-246X.2010.04819.x.

Parker, R. L. (1972), The rapid calculation of potential anomalies, *Geophys. J. R. Astron. Soc.*, *31*(4), 447–455.

Pavlis, N. K., S. A. Holmes, S. C. Kenyon, and J. K. Factor (2012), The development and evaluation of the earth gravitational model 2008 (EGM2008), *J. Geophys. Res.*, *117*, B04406, doi:10.1029/2011JB008916.

Petrunin, A., and S. V. Sobolev (2006), What controls thickness of sediments and lithospheric deformation at a pull-apart basin?, *Geology*, *34*(5), 389–392, doi:10.1130/G22158.1.

Pfister, M., L. Rybach, and S. Simsek (1998), Geothermal reconnaissance of the Marmara Sea region (NW Turkey): Surface heat flow density in an area of active continental extension, *Tectonophysics*, *291*(1–4), 77–89, doi:10.1016/S0040-1951(98)00032-8.

Pollack, H. N., S. J. Hurter, and R. Johnson (1993), Heat flow from the Earth's interior: Analysis of the global data set, *Rev. Geophys.*, *31*(3), 267–280, doi:10.1029/93RG01249.

Rangin, C., X. Le Pichon, E. Demirbag, and C. Imren (2004), Strain localization in the Sea of Marmara: Propagation of the North Anatolian Fault in a now inactive pull-apart, *Tectonics*, *23*, TC2014, doi:10.1029/2002TC001437.

Reilinger, R., et al. (2006), GPS constraints on continental deformation in the Africa-Arabia-Eurasia continental collision zone and implications for the dynamics of plate interactions, *J. Geophys. Res.*, *111*, B05411, doi:10.1029/2005JB004051.

Robinson, A., J. Rudat, C. J. Banks, and R. L. F. Wiles (1996), Petroleum geology of the Black Sea, *Mar. Pet. Geol.*, *13*(2), 195–223, doi:10.1016/0264-8172(95)00042-9.

Roecker, S., C. Thurber, and D. McPhee (2004), Joint inversion of gravity and arrival time data from Parkfield: New constraints on structure and hypocenter locations near the SAFOD drill site, *Geophys. Res. Lett.*, *31*, L12S04, doi:10.1029/2003GL019396.

Sandwell, D. T. (1987), Biharmonic spline interpolation of GEOS-3 and SEASAT altimeter data, *Geophys. Res. Lett.*, *14*(2), 139–142, doi:10.1029/GL014i002p00139.

Sandwell, D. T., and W. H. F. Smith (1997), Marine gravity anomaly from Geosat and ERS 1 satellite altimetry, *J. Geophys. Res.*, *102*(B5), 10,039–10,054, doi:10.1029/96JB03223.

Sandwell, D. T., E. Garcia, K. Soofi, P. Wessel, M. Chandler, and W. H. F. Smith (2013), Toward 1-mGal accuracy in global marine gravity from CryoSat-2, Envisat, and Jason-1, *Leading Edge*, 892–899.

Sandwell, D. T., R. D. Müller, W. H. F. Smith, E. Garcia, and R. Francis (2014), New global marine gravity model from CryoSat-2 and Jason-1 reveals buried tectonic structure, *Science*, *346*(6205), 65–7, doi:10.1126/science.1258213.

Sass, J. H., A. H. Lachenbruch, S. P. Galanis Jr., P. Morgan, S. S. Priest, T. H. Moses Jr., and R. J. Munroe (1994), Thermal regime of the southern Basin and Range Province: 1. Heat flow data from Arizona and the Mojave Desert of California and Nevada, *J. Geophys. Res.*, *99*(B11), 22,093–22,119, doi:10.1029/94JB01891.

Schmittbuhl, J., H. Karabulut, O. Lengliné, and M. Bouchon (2016), Seismicity distribution and locking depth along the Main Marmara Fault, Turkey, *Geochem. Geophys. Geosyst.*, *17*, 954–965, doi:10.1002/2015GC006120.

Seeber, L., O. Emre, M.-H. Cormier, C. C. Sorlien, C. McHugh, A. Polonia, N. Ozer, and N. Cagatay (2004), Uplift and subsidence from oblique slip: The Ganos-Marmara bend of the North Anatolian Transform, western Turkey, *Tectonophysics*, *391*(1-4), 239–258, doi:10.1016/j.tecto.2004.07.015.

Şengör, A. M. C., O. Tüysüz, C. İmren, M. Sakınç, H. Eyidoğan, N. Görür, X. Le Pichon, and C. Rangin (2005), the North Anatolian Fault: A new look, *Annu. Rev. Earth Planet. Sci.*, *33*(1), 37–112, doi:10.1146/annurev.earth.32.101802.120415.

Şengör, A. M. C., C. Grall, C. Imren, X. L. Pichon, N. Görür, P. Henry, H. Karabulut, and M. Siyako (2014), The geometry of the North Anatolian transform fault in the Sea of Marmara and its temporal evolution: Implications for the development of intracontinental transform faults, *Can. J. Earth Sci.*, *51*, 222–242, doi:10.1139/cjes-2013-0160.

Siyako, M., and O. Huvaz (2007), Eocene stratigraphic evolution of the Thrace basin, Turkey, *Sediment. Geol.*, *198*(1-2), 75–91, doi:10.1016/j.sedgeo.2006.11.008.

Smit, J., J.-P. Brun, S. Cloetingh, and Z. Ben-Avraham (2008), Pull-apart basin formation and development in narrow transform zones with application to the Dead Sea basin, *Tectonics*, *27*, TC6018, doi:10.1029/2007TC002119.

Sobolev, S. V., and A. Y. U. Babeyko (1994), Modeling of mineralogical composition, density and elastic wave velocities in anhydrous magmatic rocks, *Surv. Geophys.*, *15*(5), 515–544, doi:10.1007/BF00690173.

Sorlien, C. C., et al. (2012), Uniform basin growth over the last 500 ka, North Anatolian Fault, Marmara Sea, Turkey, *Tectonophysics*, *518–521*, 1–16, doi:10.1016/j.tecto.2011.10.006.

Tarantola, A. (2005), *Inverse Problem Theory and Methods for Model Parameter Estimation*, Soc. for Ind. and Appl. Math., Philadelphia, Pa.

Telford, W. M., L. P. Geldart, and R. E. Sheriff (1990), *Applied Geophysics*, 2nd ed., Cambridge Univ. Press, New York, doi:10.1002/gj.3350270119.

Ten Brink, U. S., Z. Ben-Avraham, R. E. Bell, M. Hassouneh, D. F. Coleman, G. Andreasen, G. Tibor, and B. Coakley (1993), Structure of the Dead Sea pull-apart basin from gravity analyses, *J. Geophys. Res.*, *98*(B12), 21,877–21,894, doi:10.1029/93JB02025.

Tiberi, C., M. Diament, H. Lyon-Caen, and T. King (2001), Moho topography beneath the Corinth rift area (Greece) from inversion of gravity data, *Geophys. J. Int.*, *145*, 797–808, doi:10.1046/j.1365-246X.2001.01441.x.

Vening-Meinesz, F. A. (1931), Une nouvelle méthode pour la réduction isostatique régionale de l'intensité de la pesanteur, *Bull. Géodésique*, *29*, 33–51.

Wang, C., F. Rui, Y. A. O. Zhengsheng, and S. T. Xingjue (1986), Gravity anomaly and density structure of the San Andreas Fault zone, *Pure Appl. Geophys.*, *124*(1), 127–140.

Wang, P. J., X. A. Xie, M. Frank, Y. G. Ren, D. F. Zhu, and X. M. Sun (2007), The Cretaceous Songliao basin: Volcanogenic succession, sedimentary sequence and tectonic evolution, NE China, *Acta Geol. Sin. English Ed.*, *81*(6), 1002–1011, doi:10.1111/j.1755-6724.2007.tb01022.x.